Research Repository

An experimental analysis of outdoor UAV localisation through diverse estimators and crowd-sensed data fusion

Research Repository link: https://repository.essex.ac.uk/39016/

Please note:

www.essex.ac.uk

An Experimental Analysis of Outdoor UAV Localisation Through Diverse Estimators and Crowd-Sensed Data Fusion

Mostafa Mohamed Ahmed[a,b], Mahmoud A. Shawky[c,*], Shady Zahran[a], Adel Moussa[d], Naser EL-Shimy[a], Adham A. Elmahallawy[e], Shuja Ansari[c], Syed Tariq Shah[f,*] and Ahmed Gamal Abdellatif[b]

[a]Department of Geomatics, University of Calgary, Calgary, Canada

[b]Department of Electronics and Electrical Communications Engineering, Air Defence Collage, Alexandria, Egypt

[c]James Watt School of Engineering, University of Glasgow, G12 8QQ, Glasgow, UK

[d]Department of Electrical Engineering, Port-Said University, Port-Said, Egypt

[e]Higher institute of Engineering and Technology, king Mariout, Alexandria, Egypt

[f]School of Computer Science and Electronic Engineering, University of Essex, Colchester, UK

ARTICLE INFO

ABSTRACT

Motivated by the challenge of achieving precise 3D outdoor localisation for unmanned aerial vehicles (UAVs) in global navigation satellite system (GNSS)-denied environments, this paper introduces an innovative technique. Integrating crowd-sensed data fusion to counter inertial navigation system (INS) drift during GNSS signal outages, the proposed method exploits diverse estimators to enhance its efficacy. A micro lightweight frequency modulated continuous wave (FMCW) radar mounted on the UAV captures ground scatterer reflections, processed via fast Fourier transform (FFT) to generate a range-Doppler map. This map facilitates forward velocity estimation during GNSS signal loss. This approach employs adaptive thresholding, image binarisation, and connected components-based techniques for target detection from a computer vision standpoint. The derived radar-based velocity fuses with magnetometer, barometer, and inertial measurement unit (IMU) data using diverse estimators like extended Kalman filter (EKF) and particle filter (PF). Real-time flight data evaluation and simulated outage periods using EKF and PF validate the outdoor localisation system. Experimental analyses demonstrate substantial improvements, enhancing 3D positioning accuracy by 99.89% and 99.83% for the initial and subsequent flights, respectively, leveraging PF to fortify the standalone INS mode during GNSS signal loss. This approach significantly enhances UAV localisation precision, particularly in challenging GNSS-denied scenarios, showcasing the potential for real-world applications.

1. Introduction

In recent years, there has been a substantial increase in the demand for unmanned aerial vehicles (UAVs), spanning various sectors, including both military and civilian applications [1]. These demands stem from the diverse range of functions these vehicles serve, including reconnaissance, disaster management, first aid delivery, firefighting, and battlefield support [2, 3]. Despite their utilities, UAVs encounter challenges, particularly in maintaining accurate positioning when operating in adverse environments, leading to disruptions in global navigation satellite system (GNSS) signals.

Navigating GNSS-denied environments poses a significant challenge for UAVs. While light detection and ranging (LiDAR) systems are often utilised as supplementary sensors, their drawbacks render them unsuitable for smaller UAVs [3]. Camera-based systems, offering advantages like compact size and low power consumption, face challenges related to lighting conditions and featureless areas. Monocular visual odometry (VO) suffers from scale ambiguity, resulting in navigation drift over time, but stereo-fixed cameras help mitigate this issue. Precise calibration of the lever arm and bore sight parameters is essential for accurate navigation configurations [4]. Integrating the inertial measurement unit (IMU) with VO helps mitigate errors and scale issues. Radar beacons and the signal of opportunity (SoP) method offer alternative approaches for GNSS-denied navigation, but practical usage is limited by installation challenges and the need to create signal strength-based maps [5]. In recent years, radar-based vehicle dynamic estimation has emerged as a promising approach for navigation tasks. Previous studies have addressed the limitations of radar-aided navigation solutions reliant on Doppler measurements. However, traditional radars' size, weight, cost, and power consumption pose significant challenges, particularly for small UAVs in navigation.

Given the reliance of UAVs on GNSS/inertial navigation system (INS) integrated measurements for localisation, the susceptibility of GNSS signals to blockage or interference introduces potential errors in the INS measurements [5, 6]. Instances, where GNSS signals become inaccessible, necessitate sole reliance on INS measurements for positioning,

thereby exacerbating the risk of rapid degradation in the navigation solution due to INS drift [6]. Integrating supplementary sensors becomes imperative to address and mitigate INS drift errors arising from GNSS signal unavailability. Consequently, this research presents a robust outdoor localisation system that harnesses crowd-sensing data fusion alongside diverse nonlinear estimators tailored for a small quadcopter operating in environments lacking GNSS signals, see Fig. 1. The outcomes and efficacy of the proposed system are supported by real-time flight data analysis.

1.1. Contributions

The following summarises the contributions of the proposed system:

1. *Enhanced precision in GNSS-denied environments*: Introducing an outdoor localisation system that offers heightened accuracy and reliability even in environments lacking GNSS signals.
2. *Utilisation of crowd-sensing data fusion and nonlinear estimators*: The methodology involves strategically integrating crowd-sensing data fusion alongside multiple nonlinear estimators. This integration aims to elevate the efficacy of outdoor localisation solutions across diverse typical manoeuvring scenarios.
3. *Real-time functionality and natural ground scatterer utilisation*: The suggested approach boasts a rapid target detection processing time of approximately 1 millisecond, emphasizing real-time functionality. Unlike prior artificial reflector-based radar localisation techniques, this proposed algorithm leverages natural ground scatterers such as trees and asphalt to enhance outdoor localisation accuracy in GNSS signal-denied situations.
4. *Addressing MEMS IMU drift and demonstrated performance*: Demonstrating the system's effectiveness in mitigating low-cost micro-electro-mechanical systems (MEMS) IMU drift issues using actual flight data. Furthermore, the proposed outdoor localisation solution undergoes testing under a 2-minute GNSS signal loss interval across two real flights, showcasing a maximum error of 8.15 meters in 3D positioning.

1.2. Use Cases and Potential Applications

The integration of advanced wireless communication systems, such as 6G, with UAVs offers significant potential across various domains. In the realm of secure vehicular communication, the enhancement provided by 6G technology and UAVs facilitates improved traffic monitoring and information exchange. UAVs equipped with IMUs, radar systems, and cameras enable secure and efficient real-time traffic analysis. This advancement leads to several key benefits. For example, precise UAV localisation significantly improves traffic pattern analysis, which in turn reduces congestion and enhances transportation efficiency. Real-time data from UAVs supports adaptive routing, allowing vehicles to navigate based on current traffic conditions. Accurate
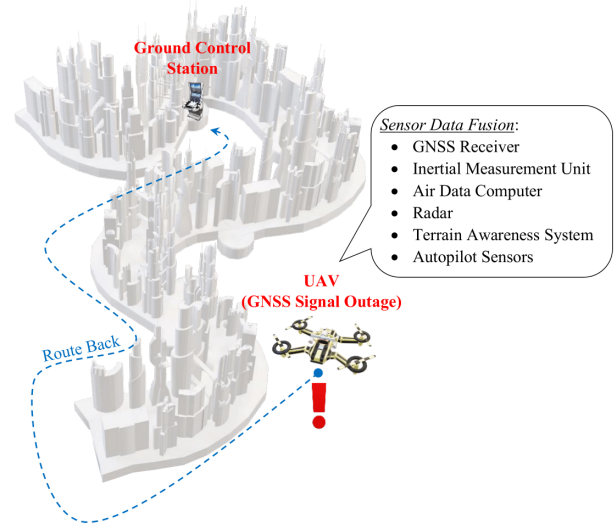

Figure 1: GNSS signal outage: Mission abort scenario.

localisation also bolsters reliable communication channels for traffic alerts and safety notifications, while UAVs provide crucial real-time hazard data that enhances roadway safety through collision avoidance systems. Additionally, the data obtained enables dynamic adjustments to traffic signals and regulations, optimising traffic flow. Figure 2 illustrates the envisioned system architecture for UAV-assisted secure vehicular communication, underscoring the critical role of high-precision UAV localisation in these applications.

Beyond vehicular communication, the proposed methodology has broad implications for various sectors. In smart city infrastructure, UAVs contribute significantly to disaster management, surveillance, and emergency coordination. They play a vital role in extending network coverage and improving connectivity in areas with limited ground infrastructure, thus enhancing network optimisation. In disaster response, UAVs facilitate real-time monitoring, search and rescue operations, and data collection in hazardous environments. Furthermore, in precision agriculture, UAVs offer detailed agricultural data, which aids in improving crop management and promoting sustainable farming practices. Lastly, UAVs support environmental monitoring by tracking air quality, wildlife, and ecosystems, thereby contributing to conservation efforts and maintaining ecological balance.

The paper's structure includes the following: Section 2 reviews the current state-of-the-art, Section 3 discusses the system architecture in detail, Section 4 presents experimental results, and Section 5 summarises findings, conclusions, and implications of the proposed system and its application.

2. Related Works

Navigating UAVs in GNSS-denied outdoor environments presents a notable challenge during mission execution. Extensive exploration of diverse sensors and methodologies has been conducted to enhance navigation solutions in GNSS-denied settings. Among these, the incorporation
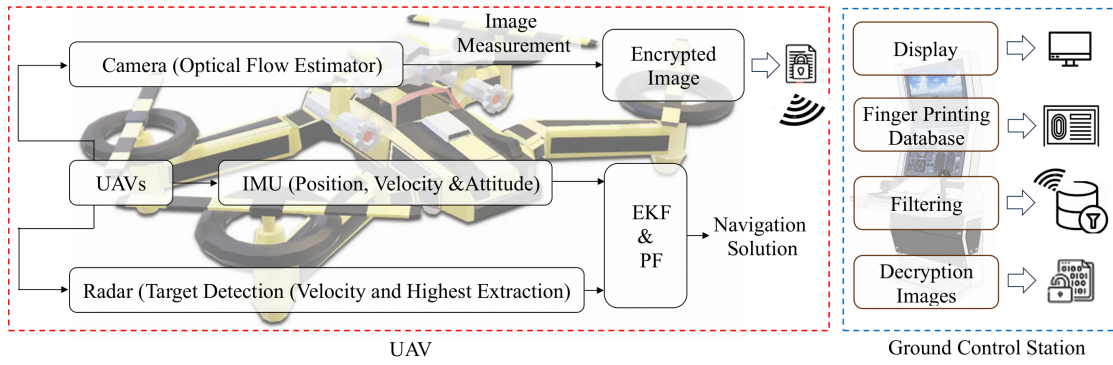
Figure 2: Envisioned system architecture for UAV-assisted secure vehicular communication.

of LiDAR equipment has been observed in select outdoor localisation systems designed for UAVs operating in environments where GNSS signals are lost [7, 8].

LiDAR systems serve as aiding sensors in GNSS-denied environments. However, their suitability for micro and miniature UAVs is limited by their weight, size, and substantial power consumption. Moreover, environmental conditions such as rain and fog can adversely affect the accuracy of laser beam readings. Visual sensors have emerged as viable components in GNSS-denied outdoor localisation systems for UAVs [9]. Onboard cameras offer advantages in compact size, lightweight nature, low power consumption, and capacity to yield valuable imagery, thereby enhancing positioning accuracy during GNSS signal disruptions. However, varying brightness, illumination discrepancies, and featureless regions can influence the quality of camera-based imaging measures. Both monocular and stereo approaches are prominent within the domain of VO. Due to its cost-effectiveness and compact design, Monocular VO holds appeal across diverse applications [10, 11]. Nevertheless, monocular VO is prone to a scale ambiguity issue that can accelerate navigation solution drift over time [12, 13, 14]. To address this limitation, the utilisation of stereo-fixed cameras featuring overlapping fields of view has been explored [15, 16, 17].

Other research endeavours have combined IMUs with VO to address INS drift errors and counteract the scale ambiguity issue [18]. In environments lacking GNSS signals, radar beacons emerge as an alternative method for outdoor localisation. These beacons possess predetermined locations that act as reference points across the localisation area [19]. While offering high accuracy in outdoor localisation, installing radar beacons across large regions presents challenges, limiting their applicability in GNSS-denied environments. Conversely, certain GNSS-denied outdoor localisation systems adopt an SOP approach, utilising available signals such as AM radio [20], Wi-Fi [21], digital, and analogue television to compute localisation solutions. However, SOP primarily relies on mapping the area based on the strength of received signals [22, 23, 24].

The SOP-based approach entails mapping areas while GNSS signals are accessible, utilising this map for subsequent outdoor localisation during GNSS signal outages. However, a significant drawback of the SOP method is its inability to provide localisation solutions in unmapped areas. An alternative technique for outdoor localisation in GNSS-denied environments is the traditional multi-trilateration approach. This method necessitates knowledge of signal source positions and signal time of arrival (TOA). Yet, a notable drawback lies in the necessity to pre-survey transmitter positions, which may pose challenges in areas that need to be prepared for outdoor localisation applications [25].

Over the past decades, constraints related to size, weight, cost, and power consumption have impeded the widespread application of radars in outdoor localisation, especially concerning small UAVs [26]. However, advancements in radar technologies have led to the development of new iterations that address the limitations of their predecessors, rendering them more compatible with diverse mobile mapping and localisation functions on miniature UAVs. Examples include synthetic aperture radar (SAR) systems tailored for such applications [27].

Furthermore, radar-based navigation systems exhibit resilience against environmental disruptions like rain, dust, and fog. Kauffman et al. [27] conducted simulations of an aerial navigation system employing ultra-wideband orthogonal frequency division multiplexed (UWB-OFDM) radar in GNSS-denied environments. Target detection utilised the M/N detector algorithm while tracking used the global nearest neighbour (GNN) tracker. An outdoor localisation solution was formulated by integrating INS data with radar range measurements through an extended Kalman filter (EKF). Addressing GNSS-denied settings for small UAVs, Quist et al. [28] proposed an RO/INS integrated navigation system. The system incorporated a side-looking SAR atop the UAV for ground target identification. Employing the Hough transform [29], hyperbolic objects in the radar range-compressed image were located. These identified targets were utilised to determine along-track and cross-track velocities and altitude above ground. Diverse estimators fused predicted velocities and altitudes from the radar imagery.

Gamal et al. [30] introduced a methodology that integrates IMU and Wi-Fi-based received signal strength indicator (RSSI) measurements. This approach employs sensor fusion, Wi-Fi fingerprinting, and dead reckoning techniques to enhance indoor localisation accuracy. The methodology was evaluated by experimentally comparing estimated paths with predefined reference paths. In reference [31], Kaur et al. utilised a grid approach with channel state information (CSI) fingerprinting and machine learning methods to improve indoor localisation by determining the location of a mobile device, and compared the accuracy of this method, based on RSSI and channel phase response, against heuristic approaches like DOA estimation through experiments conducted in a standard indoor setting. Tariq et al. in [32] extended the work introduced in [31] by investigating the effect of integrating reconfigurable intelligent surfaces (RIS) to improve the RSSI in each position, enhancing the localisation accuracy. A comprehensive experimental analysis is conducted, evaluating the accuracy of various machine learning algorithms under different RIS states, antenna types, and communication setups. This demonstrates that incorporating RIS can significantly enhance localisation accuracy, achieving an 82.4% success rate.

Karunanithy in [33] proposed a reliable data collection mechanism (RDCM) using six directional antennas to create an omnidirectional radiation pattern for node localisation and data collection in wireless sensor networks (WSNs), utilising received signal strength (RSS), angle of arrival (AoA), and coordinate values from a single anchor node, and implemented a local sink (LS)-based information collection mechanism with modified geographic routing, demonstrating superior performance in packet delivery ratio, energy consumption, and end-to-end delay compared to traditional approaches. Kong et al. [34] proposed a hybrid indoor positioning method that combines Bluetooth low energy (BLE) and pedestrian dead reckoning (PDR) using adaptive feedback extended Kalman filter (AFEKF). This method fuses BLE position, orientation, and range measurement data with PDR localisation results to enhance positioning accuracy in scenarios with low access point (AP) deployment density. Its effectiveness was demonstrated through experiments conducted in large underground parking lots.

3. System and Scheme Modeling

This section comprehensively discusses the system architecture and the proposed method in detail.

3.1. System Architecture

The designed for the proposed localisation system involves demonstrating the data flow, processing steps, and decision-making. The following outlines the interactions between different layers:

1. *Sensor data processing flow*: Following are the various data processing types involved in this step:
   (a) IMU data processing (*proc_imu*): This process begins with the calibration step designed to compensate for inherent sensor errors such as biases, scale factors, and misalignments. Noise filtering techniques, including Kalman filters or low-pass filters, are applied to minimize noise from accelerometer and gyroscope measurements. Additionally, algorithms for bias compensation are implemented to remove systematic errors. Fusion with other sensors, like GNSS or barometer data, is performed using advanced fusion algorithms like the EKF or PF to enhance accuracy and reliability.
   (b) GNSS data processing (*proc_gnss*): This process initiates with signal reception mechanisms that involve acquiring and tracking satellite signals, evaluating signal strength, and assessing signal quality. Signal processing algorithms extract critical information such as position, velocity, and timing from received GNSS signals, incorporating techniques to estimate and correct various error sources like multipath effects, and ionospheric or tropospheric delays, ensuring accurate navigation solutions.
   (c) Barometer and radar data processing (*proc_baro*): This process involves algorithms converting atmospheric pressure readings into altitude estimates, employing barometric formulas or models. Compensatory techniques may account for temperature effects on pressure measurements if necessary. Radar data processing focuses on deriving range and velocity information from received radar signals, utilising sophisticated algorithms to reduce clutter and noise through techniques like constant false alarm rate (CFAR) or fast Fourier transform (FFT), ensuring accurate target detection and tracking in challenging environments.
2. *Data processing layer (process_rad)*: This layer comprises different processes described as follows:
   (a) Signal processing blocks: For each sensor, there are specific signal processing algorithms to extract relevant information from raw sensor data.
   (b) Sensor fusion algorithms (*sens_fuse*): Employed to combine information from multiple sensors to produce a more accurate estimation of the vehicle's state.
   (c) Object detection and tracking: Algorithms to detect and track objects using radar or other sensing modalities.
3. *Localisation and estimation layer (loc_map)*:
   (a) EKF/PF: Used for state estimation and sensor fusion. They incorporate sensor data, system dynamics, and error models to estimate the vehicle's state.
   (b) Localisation Algorithms: Combining GNSS, IMU, and other sensor data for precise localisation.
   (c) Environment Modeling: Mapping and localisation techniques to represent the surrounding environment.

Algorithm 1 System Operations

```
1: Initialise Variables and System Parameters
2: Init_sys()
3: while sys_run do
4:     Sensor Data Processing
5:     imu ← proc_imu(raw_imu)
6:     gnss ← proc_gnss(raw_gnss)
7:     baro ← proc_baro(raw_baro)
8:     rad ← proc_rad(raw_rad)
9:     Sensor Fusion and Localisation
10:    fused ← sens_fuse(imu, gnss, baro, rad)
11:    est_state ← loc_map(fused)
12:    Control and Decision-Making
13:    ctrl_cmds ← make_ctrl(est_state)
14:    exec_cmds(ctrl_cmds)
15:    Safety and Redundancy Checks
16:    check_safe_redun(est_state, sens_data)
17:    Communication and Interface
18:    trans_data(est_state)
19:    recv_cmds()
20:    upd_vis(est_state)
21: end while
```

where **Init_sys**: Initialise the System; **sys_run**: System Running; **imu**: IMU Data; **proc_imu**: Process IMU Data; **raw_imu**: Raw Data from the IMU; **gnss**: GNSS Data; **proc_gnss**: Process GNSS Data; **raw_gnss**: Raw Signals from the GNSS; **baro**: Barometer Data; **proc_baro**: Process Barometer Data; **raw_baro**: Raw Readings from the Barometer; **rad**: Radar Data; **proc_rad**: Process Radar Data; **raw_rad**: Raw Signals from the Radar; **sens_fuse**: Sensor Fusion; **fused**: Fused Data; **est_state**: Estimated State; **loc_map**: Localisation and Mapping; **ctrl**: Control; **cmds**: Commands; **exec_cmds**: Execute Commands; **Redun**: Redundancy; **check_safe_redun**: Check Safety and Redundancy; **Comm**: Communication; **trans_data**: Transmit Data; **recv_cmds**: Receive Commands; **upd_vis**: Update Visualisation
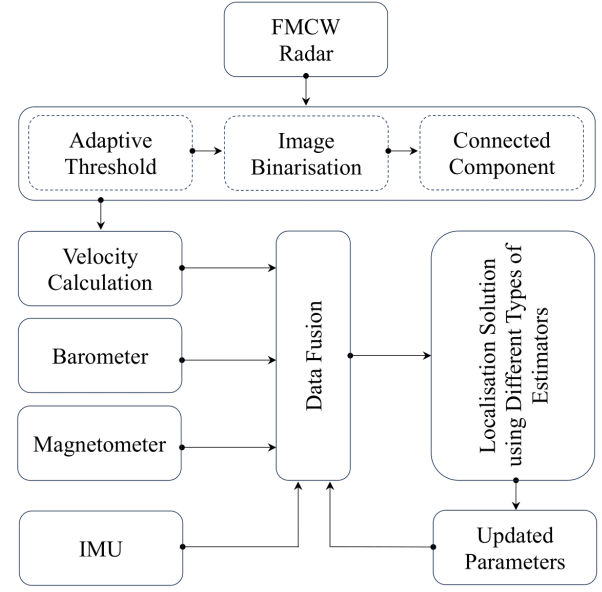

Figure 3: The block diagram of the proposed method.

4. *Control and decision layer (make_ctrl)*: This layer comprises the following algorithms.

   (a) Path planning: Algorithms for planning optimal paths based on localisation data and mission objectives.

   (b) Control systems: responsible for controlling the vehicle based on the estimated state, such as an autopilot or guidance system.

   (c) Decision-making logic (*exec_cmds*): Processing of localisation data to make decisions, such as avoiding obstacles or maintaining a specific trajectory.

5. *Communication layer*: This layer involves these steps.

   (a) Interfacing and communication (*trans_data*): Handling the exchange of data between different modules within the system.

   (b) Interface with external systems (*recv_cmds*): Connection points for communication with ground stations or external control systems.

6. Visualisation and user interface (*upd_vis*): Involves data display and user-friendly interfaces for monitoring, configuring, and interacting with the system.

7. *Redundancy and safety measures (check_safe_redun)*: Includes duplicate components or sensors for fault tolerance and safety protocols for emergencies or system failures.

Algorithm (1) illustrates the sequential steps involved in the proposed system.

3.2. Scheme Modelling

The proposed method aims to enhance the 3D outdoor localisation precision of UAVs in GNSS-denied environments through frequency-modulated continuous wave (FMCW) radio odometry (RO) technology. This system enhances reliability and accuracy in the absence of GNSS signals. Utilising FMCW RO, the outdoor localisation system integrates data from barometers and magnetometers, commonly present on UAVs, as additional assisting sensors. The process involves fusing the estimated longitudinal velocity component with IMU and magnetometer measurements using nonlinear estimators like EKF and PF. Fig. 3 illustrates the system block diagram, comprising key stages: data capture, target identification, velocity extraction, and integration of RO/INS/magnetometer/barometer data into various types of nonlinear estimators.

The EKF is advantageous for its computational efficiency and optimal performance under linear and Gaussian assumptions, making it suitable for low-dimensional state spaces commonly encountered in UAV applications. However, it has limitations in handling strong nonlinearities and non-Gaussian noise. Conversely, the PF excels in managing highly nonlinear systems and non-Gaussian noise through its ability to represent multimodal distributions, though it requires higher computational resources. The decision between EKF and PF hinges on the specific characteristics of the system dynamics, measurement models, and available computational resources. For our application, the EKF is employed where nonlinearities are mild, and the PF is used in scenarios with significant nonlinearities and non-Gaussian noise, such as highly manoeuvring UAVs or GNSS-denied environments.

3.2.1. Radar Data Acquisition

In order to obtain range and velocity measurements, the proposed system initially processes internal radar signals through a micro FMCW radar. This radar emits frequency-modulated chirps (f_{RFTX}) with a sawtooth-shaped frequency modulation during flights over an uncharted area.

These signals interact with ground objects, get reflected, and are received by the radar. The Doppler effect, caused by the movement of objects, induces a frequency shift between the transmitted and received signals, allowing estimation of the target's radial velocity. The time delay between transmission and reception is also used to estimate the target's range. The radar module internally processes these signals to extract range and velocity data, which are then transmitted to a ground station for further processing and fusion with data from other sensors. The f_{RFTX} can be formulated as

$$f_{RFTX} = f_0 + K_f t, \qquad 0 \le t < T \qquad (1)$$

where f_0 is the initial transmitted frequency, K_f represents the sweep rate, and T is the frequency sweep time. The frequency sweep rate in (1) can be expressed as:

$$K_f = \frac{BW}{T} \qquad (2)$$

where the transmitted signal bandwidth is denoted as BW. The radio frequency (RF) signals experience a slight frequency Doppler shift Δf and a round-trip propagation delay time Δt as the radar signal travels to the scatterers and returns to the radar's reception antennas. These effects, caused by range propagation, lead to these time delays and frequency shifts. For each reflector i, the difference in time between transmitted and received signals can be described as:

$$\Delta t = 2\frac{r_i}{c} \qquad (3)$$

where r_i signifies the distance between the radar antenna and each scatterer within the radar's beam width. The range is defined as the cumulative distance encompassing the radar antenna and the individual scatterers, and c symbolises the speed of light. The frequency of the receiving signal (f_{RFRX}) is altered in proportion to the time delay Δt, and can be expressed as:

$$f_{RFRX} = f_0 + K_f(t - \Delta t), \qquad \Delta t \le t < T + \Delta t \qquad (4)$$

The integration of the transmitted and received signals yields a mixed signal. This mixed signal undergoes low-pass filtering to extract the video signal $x(t)$. This signal, characterized by a low rate of change, is referred to as the beat frequency f_b, and its expression is given by:

$$f_b = K_f \Delta t \qquad (5)$$

By substituting (3) in (5), f_b can be rewritten as:

$$f_b = \frac{BW}{T} \cdot 2\frac{r_i}{c} \qquad (6)$$

3.3. Target Detection and Velocity Extraction

CFAR is a pivotal radar signal processing method employed in identifying targets within cluttered environments, ensuring a minimized false alarm rate [36]. Its fundamental objective lies in dynamically computing threshold power levels to ascertain the presence of a target within a designated cell. CFAR operates by comparing the signal power within the cell under test (CUT) against neighbouring cell power levels within a local neighbourhood, thereby facilitating target detection. Distinct CFAR methodologies such as cell averaging (CA), greatest-of-cell averaging (GOCA), smallest-of-cell averaging (SOCA), and ordered statistics CFAR (OS-CFAR) diverge in their approaches to estimate threshold power levels based on neighbouring cell power measurements [37]. In CA-CFAR, the threshold is derived from the average power of adjacent cells, while GOCA identifies the threshold from the maximum power among neighboring cells. In contrast, SOCA determines the threshold from adjacent cells' minimum power, and OS-CFAR uses statistical techniques to order neighboring cell power levels to set the threshold accordingly [38]. The CFAR adaptive thresholding, contingent upon neighboring cell power levels, enables the differentiation between target signals and environmental clutter. Consequently, CFAR emerges as an indispensable tool across diverse radar applications [39].

Upon receiving the radar signal, the Doppler frequency $f_{Doppler}$ is extracted from the signal's phase changes, offering insight into the object's velocity relative to the radar. Two-dimensional (2D) signal processing techniques are employed on the spectrum of the extracted signal to derive range and velocity details for each scatterer. This involves utilising methods like FFT to construct a range-Doppler map (RDM), displaying signal strength from diverse earth scatterers across different ranges and velocities. In the context of the radar system described, the RDM is crafted by employing 256 samples per chirp, sampled at a rate of 264 nanoseconds, and processing the signals received through three receiving antennas. The resultant RDM is obtained by averaging the RDM data from all antennas, generating a 256×256 pixel map with a 32-bit amplitude value assigned to each pixel. This visualization showcases detected targets and their velocities, with the horizontal axis denoting speed measurements and the vertical axis representing range measurements. Each pixel within the RDM carries a 32-bit value indicative of the received signal strength from various earth scatterers. Subsequently, the RDM image serves as the basis for target detection and velocity extraction. This can involve thresholding, clustering, or template matching tailored to specific application needs and requirements [40, 41].

The experimental analysis identifies targets through CFAR in the RDM image depicted in Fig. 4, with the outcomes presented in Fig. 5. However, the detection process captures only a portion of the reflected arc from ground targets, leaving the remainder undetected. Furthermore, CFAR erroneously identifies a false alarm (noise) exhibiting a power level distinct from its adjacent cells. One of the encountered challenges involves estimating the power level of
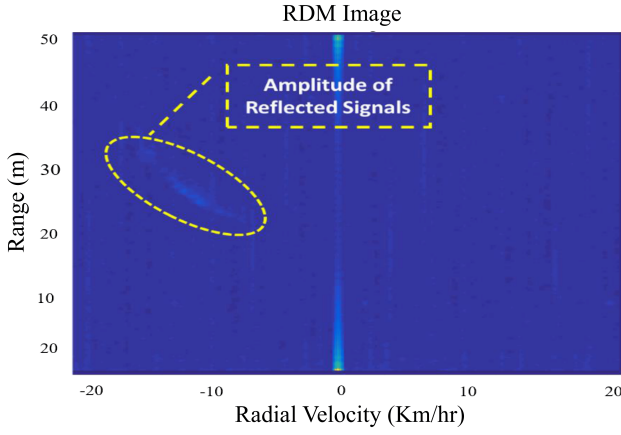
RDM Image

Figure 4: The RDM picture of the ground reflected signals.

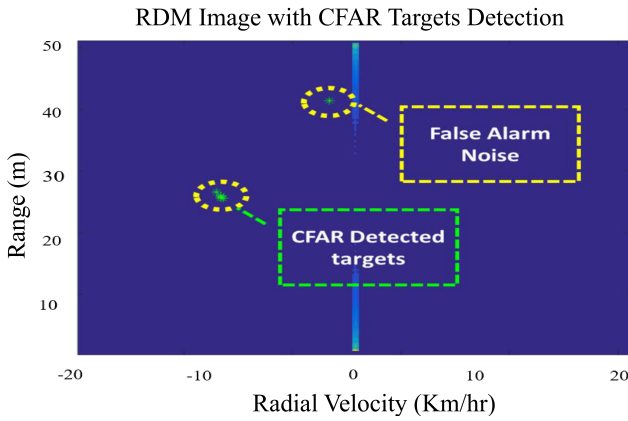## RDM Image with CFAR Targets Detection

Figure 5: Identifying targets in RDM images using CFAR.

the CUT concerning its background, particularly in regions hosting clustered real ground scatterers. In such scenarios, the CFAR algorithm encounters difficulty in detecting all targets due to the similarity in power intensity between the CUT and its neighboring cells, creating challenges in differentiation.

The second issue associated with CFAR involves potential false alarms arising from radar measurement noise, which might exhibit relatively higher power levels than their neighboring cells. In environments with low signal-to-noise ratio (SNR), distinguishing between noise and genuine targets within the RDM image can pose challenges. To mitigate this concern, an alternative solution involving an adaptive global thresholding technique has been proposed. This technique entails computing a global histogram for the entire RDM image and leveraging it to estimate the threshold level for each epoch. The adaptive threshold is determined based on a specified confidence level derived from the distribution's mean value. This approach is designed to improve target detection accuracy while reducing noise-induced false alarms in low SNR environments.

To create a binary image for target detection, an adaptive threshold is computed using a confidence level set at seven times the standard deviation of the histogram analysis, see Fig. 6(a). This adaptive threshold facilitates differentiation between robust ground scatterers surpassing the threshold and the cluttered or noisy background within the image. Pixels above this adaptive threshold are assigned a value of "1" in the binary image, while all other values are designated as "0", see Fig. 6(b). A connected component-based approach is adopted to accumulate neighboring pixels with values of "1" into certain areas, deviating from a local maxima-based method, see Fig. 6(c). Subsequently, the centroid of each region is determined by averaging its surrounding pixels along both the X and Y axes. The resulting X-axis of the binarized RDM displays the radial velocity for each identified target. Meanwhile, the averaging method yields the drone's resultant longitudinal velocity in the body frame. Fig. 6 shows the conclusive images obtained from this technique.

3.4. Multi-Sensors Data Fusion

This section presents the fusion process of crowd-sensing data derived from diverse sensors, including INS, magnetometers, barometers, radar, and GPS. Nonlinear estimators such as EKF and PF are employed for this fusion process. Localisation states, portrayed within the localisation (n-frame), are acquired by processing raw data from the IMU using the aforementioned nonlinear estimators. These estimators use a state vector represented as

$$x = \begin{bmatrix} \delta r^n_{1\times3} & \delta v^n_{1\times3} & \epsilon^n_{1\times3} & b_{1\times3} & d_{1\times3} & s_{a_{1\times3}} & s_{g_{1\times3}} \end{bmatrix} \quad (7)$$

where δr^n, δv^n, and ϵ^n represent INS error states in the location, velocity, and attitude, respectively. Meanwhile, b and d represent the estimated bias in both accelerometers and gyros, respectively. Finally, the accelerometer and gyroscope scale factors are represented by s_a and s_g. The fusion of different sensors is performed in a loosely coupled fashion through two sequential procedures within the nonlinear estimators. The initial phase entails predicting navigation states based on IMU measurements, followed by subsequent stages involving measurements and observations. The upcoming subsections elaborate on the specific procedures within this process.

3.4.1. Prediction Model

The formulation of the error states within the INS over time can be expressed as follows:

$$\bar{x}_{k+1} = \Phi_k \hat{x}_k + G_k w_k \quad (8)$$

where Φ_k, x_k, G_k, and w_k represent the state transition matrix, the error vector, the matrix containing the noise coefficient, and the system noise, respectively. The utilisation of first-order Gauss-Markov characterizes the representation of INS stochastic errors. Therefore, the prediction of P_k at any epoch can be expressed as:

(a) Adaptive thresholding optimsation using histogram analysis (Mean: 18.6347 and std: 2.8319).

(b) Binarised RDM image using the optimised threshold.

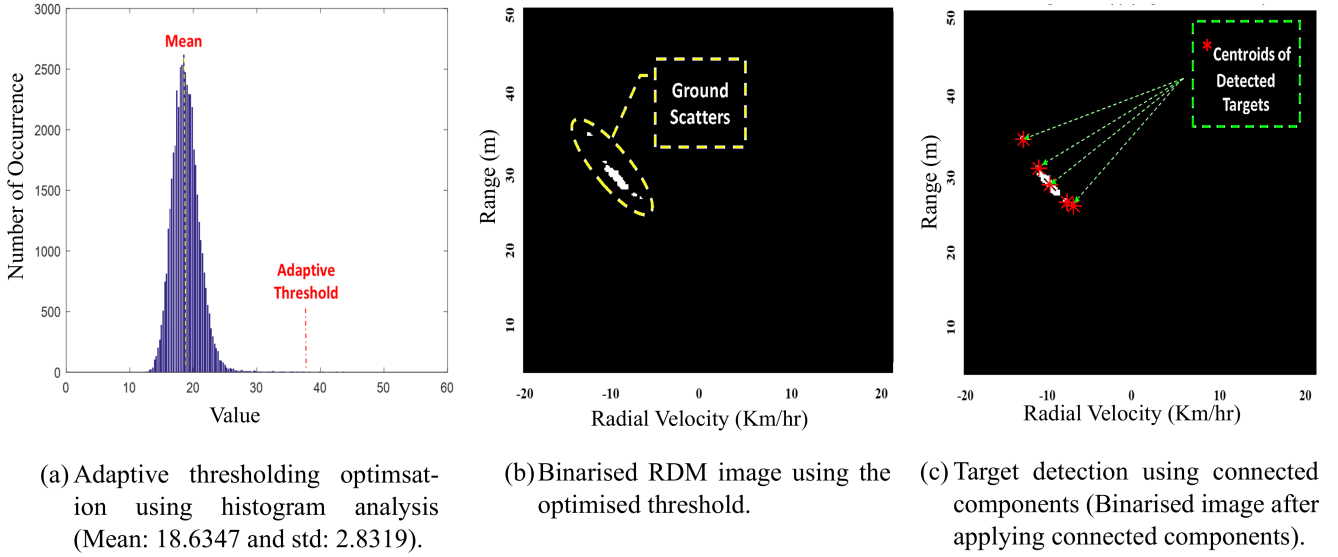(c) Target detection using connected components (Binarised image after applying connected components).

Figure 6: Adaptive thresholding technique for target detection in low SNR environments.

$$\bar{P}_{k+1} = \Phi_k P_k \Phi_k^T + \bar{G}_k Q_k \bar{G}_k^T \tag{9}$$

where $\bar{P}_{k+1}$ is the predicted error covariance matrix at the time step $(k+1)$ P_k, and Q_k are the error covariance matrix, and the covariance matrix of the process noise at time step k, respectively.

3.4.2. Crowd-Sensing Measurements

The INS state estimation undergoes an update process leveraging the positional information provided by the GNSS signal, denoted as P_{GNSS}^{ned}. This information pertains to the North-East-Down (NED) coordinates derived from GNSS positioning and is described as follows:

$$P_{GNSS}^{ned} = [\ P_{n,GNSS} \quad P_{e,GNSS} \quad h_{GNSS}\ ] \tag{10}$$

where $P_{(n,GNSS)}$ and $P_{(e,GNSS)}$ refer to the North and East position components, respectively, while h_{GNSS} denotes the ellipsoidal height. The barometer contributes to the height update (h_{baro}), and in conjunction with raw magnetometer measurements, aids in updating the heading angle (ψ_{mag}) as follows:

$$\psi_{mag} = \tan^{-1}\left(\frac{-M_y \cos\phi + M_z \sin\phi}{M_x \cos\theta + (M_y \sin\phi + M_z \cos\phi)\sin\theta}\right) + \delta_{mag} \tag{11}$$

where the vector $[\ M_x \quad M_y \quad M_z\ ]$ denotes the magnetic field measurements observed within the body-frame. The variables ϕ and θ correspond to the roll and pitch angles, respectively. Additionally, δ_{mag} signifies the magnetic deviation with respect to the true north.

3.4.3. Observation Model

In the process of updating the nonlinear estimators with measurements, the disparity between INS and GNSS measurements within the navigation frame is computed. However, due to the lever-arm effect resulting from the differing positions of the GNSS antenna and the onboard IMU, it is crucial to rectify this effect before updating the nonlinear estimators. This rectification involves aligning the IMU center with the GNSS antenna center via a compensatory procedure, represented as follows:

$$\hat{P}_{GNSS}^{ned} = \hat{P}_{IMU}^{ned} + D^{-1} C_b^l l_{GNSS}^b \tag{12}$$

$$D^{-1} = \begin{bmatrix} \frac{1}{R_M + h} & 0 & 0 \\ 0 & \frac{1}{(R_N + h)\cos\phi} & 0 \\ 0 & 0 & -1 \end{bmatrix} \tag{13}$$

$$R_M = \frac{R\left(1 - e^2\right)}{\left(1 - e^2 \sin^2\phi\right)^{3/2}} \tag{14}$$

$$R_N = \frac{R}{\left(1 - e^2 \sin^2\phi\right)^{1/2}} \tag{15}$$

where $\hat{P}_{GNSS}^{ned}$ and $\hat{P}_{IMU}^{ned}$ represent the positions of the GNSS antenna and IMU in the body frame, respectively, calculated based on their respective center positions. The lever arm connecting the GNSS antenna and IMU is denoted by l_{GNSS}^b. The rotation matrix transforming the body frame to the local level frame is denoted as C_b^l. Within this context,

the Earth's radius is symbolized by R, the eccentricity of the elliptical planet by e, and the latitude by ϕ. The GNSS position measurements are expressed as follows:

$$\tilde{P}_{GNSS}^{ned} = P_{GNSS}^{ned} + D^{-1}e_P \quad (16)$$

where e_P represents the positioning error resulting from GNSS measurements, while the attitude errors are denoted by φ. These attitude errors are encapsulated in a skew-symmetric matrix, formulated as follows:

$$\varphi = \begin{bmatrix} 0 & -\epsilon_d & \epsilon_e \\ \epsilon_d & 0 & -\epsilon_n \\ -\epsilon_e & \epsilon_n & 0 \end{bmatrix} \quad (17)$$

where ϵ_n, ϵ_e, and ϵ_d represent the attitude mistakes in the directions of North, East, and Down. Thus, the positioning measurements utilised for an EKF update derived from (16) and (17) can be formulated as:

$$z_{GNSS} = D\left(\hat{P}_{GNSS}^{ned} - \tilde{P}_{GNSS}^{ned}\right)$$
$$= \begin{bmatrix} I_{3\times3} & \vdots & 0_{3\times3} & \vdots & C_b^l l_{GNSS}^b & \vdots & 0_{3\times12} \end{bmatrix} x - e_P \quad (18)$$

After obtaining the measurement update z_{GNSS} from the differences between the estimated and true GNSS positions, the next stage involves utilising the computed residuals δz_k and the corresponding design matrices H_k associated with the onboard sensors. These residuals represent the discrepancies between predicted and actual measurements. The design matrices encapsulate the linearisation of the measurement model for the nonlinear estimator. Leveraging these residuals and design matrices, the nonlinear estimators gain K_k is computed, facilitating the refinement of the state estimate $\hat{x}_k^+$ and its covariance matrix P_k^+. The gain K_k denotes the optimal weight applied to the measurement update z_{GNSS} in the estimation process. It enables the correction of the state estimate, enhancing its accuracy considering the available sensor information.

$$K_k = P_k^- H_k^T \left(H_k P_k^- H_k^T + R_k\right)^{-1} \quad (19)$$

$$\hat{x}_k^+ = \hat{x}_k^- + K_k \delta z_k \quad (20)$$

$$P_k^+ = \left(I - K_k H_k\right) P_k^- \quad (21)$$

where K_k is calculated using the predicted state estimation error covariance matrix P_k^- and the transpose of the design matrix H_k associated with sensor measurements, and the measurement noise covariance R_k. The updated state estimation at time step k, represented by $\hat{x}_k^+$, emerges from the addition of the predicted state estimation $\hat{x}_k^-$ and the Kalman gain K_k multiplied by the residuals δz_k, which reflect the differences between predicted and actual measurements. Additionally, the updated state estimation error covariance matrix P_k^+ is determined through the adjustment of the predicted covariance P_k^- by the Kalman gain K_k and the design matrix H_k, resulting in a refined estimation of the state and its associated uncertainty at time step k.

4. Experimental Results and Discussion

This section discusses the experimental parameters and analytical methodologies employed to validate the effectiveness of the proposed approach.

4.1. Experimental Overview

The implemented system operates using fused simulated data, adhering strictly to flight parameters, encompassing straight, level flight at consistent velocities over flat terrain. Measurements of velocity, altitude, azimuth angle, and turn rate are utilised to update various nonlinear estimators, including the EKF and PF. Performance assessment involves simulated trajectories with diverse manoeuvring angles. Practical testing is conducted in a GNSS-denied environment over a 60-second duration, leveraging an affordable navigation-grade IMU to enhance the precision of the proposed outdoor localisation system. This flight test involved affixing a SAR to a Cessna aircraft to collect relevant data. To gauge system performance using consumer-grade IMUs typical in small UAVs, the deliberate introduction of random noises and biases into IMU measurements is undertaken. Evaluation of matched points is achieved through M-estimator sample consensus (MSAC), employing a two-step iterative process involving hypothesis generation and computation. Initially, MSAC randomly selects a subset of data and computes model parameters from this sample. Subsequently, data exhibiting errors within a predefined threshold from a hypothesis are identified as inlier candidates for object detection and tracking. The proposed outdoor localisation solution integrates altitude above ground, digital compass heading, range to scatterers, and turn rate data with a navigation-grade IMU, employing EKF and PF methodologies.

The application of the CFAR algorithm [35] facilitates target detection, while the multiple-target tracker (MTT) leverages the GNN algorithm to track these identified targets. Extracting the vehicle's relative translation and rotation is achieved by analyzing the tracked targets through the stratifying singular value decomposition (SVD) algorithm. Altitude information is derived by vertically projecting the first ground echo at a tilting angle. The proposed system adopts both loosely and tightly coupled techniques for RO and INS integration. The former estimates heading and pose variation using RO, updating the EKF and PF. While the latter employs track range and bearing as measurement updates. System evaluation spans two flights conducted in distinct areas. The first flight involves a forward-looking radar, while the second flight employs a pitched radar angle of 20 degrees, navigating through various objects like cars.
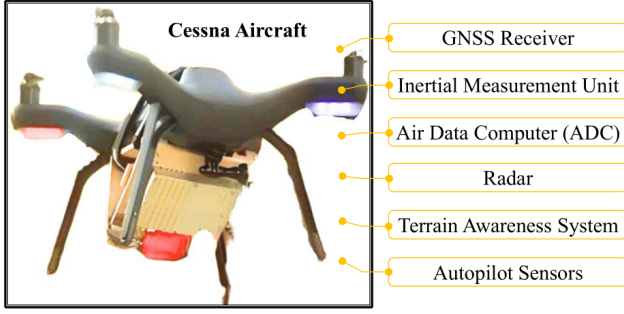
Figure 7: The integrated 3DR Solo quadcopter within the experimental configuration.
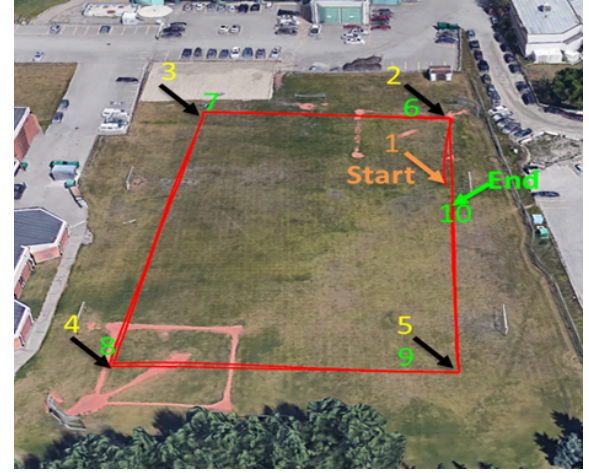

Figure 8: The waypoints of the first flight trajectory.

Fig. 7 shows the 3DR Solo quadcopter integral to the proposed system. This quadcopter is primarily governed by a Pixhawk-2 autopilot and features a suite of sensors, including an InvenSense MPU-6000 MEMS IMU, an MS5611 barometer, and a U-blox GPS. These sensors relay critical information on attitude, altitude, and position to the autopilot, ensuring stability and facilitating navigation to specified destinations. Additionally, the quadcopter incorporates a micro-FMCW radar specifically tailored to enhance outdoor localisation capabilities in GNSS-denied environments. The equipment and devices in this setup are specifically employed to optimise the performance of the 3DR Solo quadcopter when operating in areas with limited GNSS signal availability.

The FMCW radar operates at a frequency of 24 GHz and includes one transmitter and one receiver, each equipped with three microstrip patch antennas. With a resolution of 0.1 degrees, it covers ± 10 degrees in the Elevation-plane and ± 15 degrees in the Azimuth-plane. This radar, boasting a one-meter resolution, detects vehicles up to 300 meters away and individuals up to 100 meters away. Its reliability surpasses visual sensors, offering resistance to environmental factors like rain, fog, dust, and featureless terrain. Additionally, its compact size, lightweight, and low power consumption render it suitable for installation on small UAVs, enabling diverse mobile mapping and localisation applications.

In the experimental analysis, factors such as attenuation, scattering, signal distortion, Doppler effect, and antenna performance can impact the range, sensitivity, accuracy, and target tracking capabilities of a radar system. In adverse weather conditions like rain, fog, or wind, these factors can lead to decreased signal strength, increased background noise or clutter, distorted measurements, and difficulties in distinguishing between desired targets and false detections. To address these challenges and ensure reliable and accurate radar operations in various weather conditions, careful calibration, signal processing techniques, and algorithms are employed. The main advantage of the 24-GHz micro-FMCW radar by RFbeam lies in its immunity to changes in illumination and environmental conditions. Additionally, the radar system is calibrated before experimentation, employs an advanced signal processing method, and operates under appropriate conditions to achieve the desired results.

The experimental trials spanned across two days, covering distinct paths while inclining the radar at a 60-degree vertical angle from the quadcopter body. Furthermore, two real flights were conducted in separate locations to evaluate the efficacy of the proposed methodology. The following outlines the two trials of the executed experiment.

4.2. The First Experimental Trial

In this experimental trial, a flight is conducted utilising the 3DR Solo quadcopter equipped with a micro-FMCW radar. The flight path comprises two laps encompassing ten waypoints, maintaining a maximum speed of 5 m/s and lasting a total duration of 155 seconds, depicted in Fig. 8. During the flight, data is collected concerning the quadcopter's forward velocity. This observed velocity is then compared with the computed velocity derived from radar data using the proposed method. Fig. 9 illustrates the validation process for the suggested approach in computing velocity through micro-FMCW radar. The comparison results demonstrate a notable alignment between the observed and computed velocities.

Based on the available data, the proposed RO system demonstrates an ability to estimate a root mean square error (RMSE) of 1.2 m/s for forward vehicle velocity, as depicted in previous figures. To further assess the system's performance, five scenarios of GNSS signal outages are executed, varying in duration from 45 to 135 seconds. The initial outage lasted for 45 seconds. Fig. 10 and 11 present the differentiation between the computed 2D flight path during the initial flight's outage segments, as determined by the proposed system, and the ground truth obtained through GNSS/INS fusion. Specifically, Fig. 10 presents the comparison during a 45-second GNSS signal outage, while Fig. 11 illustrates the comparison during a 135-second outage. These comparative analyses serve to evaluate the precision and reliability of the suggested RO system for
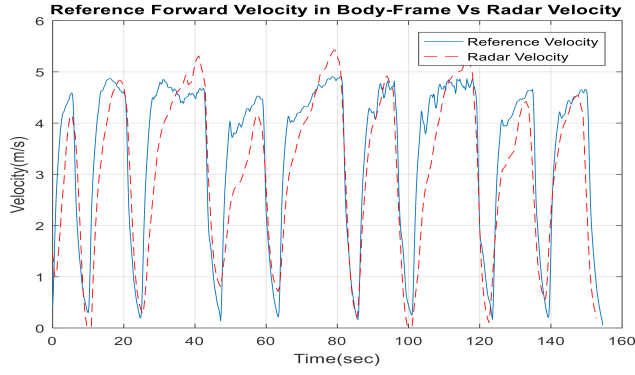
Figure 9: Comparison between the reference acquired velocity by the (GNSS/INS) fusion, and computed velocity by the proposed system.

Figure 10: Comparison between the reference acquired velocity by the (GNSS/INS) fusion, and computed velocity by the proposed system.
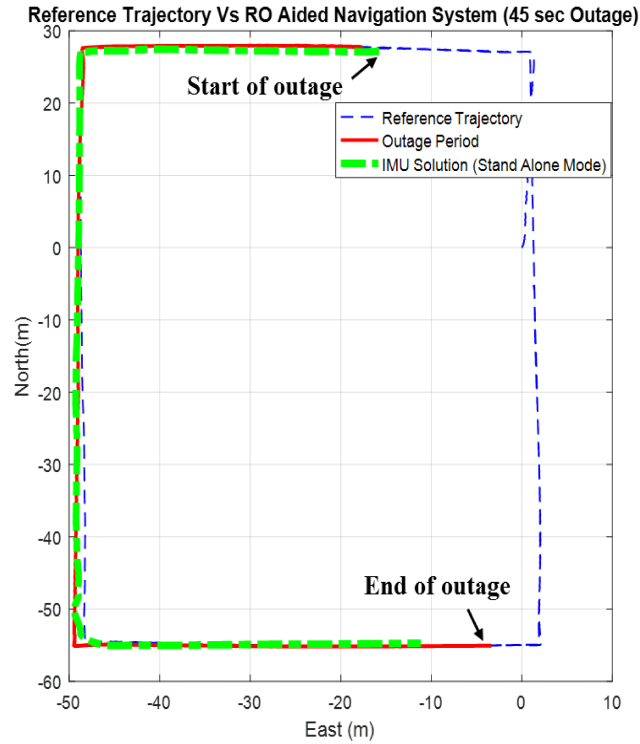

Figure 11: Comparison between the reference acquired velocity by the (GNSS/INS) fusion, and computed velocity by the proposed system.

outdoor localisation, especially when navigating trajectories during periods of GNSS signal loss.

Fig. 12 shows the capability of the proposed RO system in mitigating INS drift during GNSS signal loss, resulting in a maximum error of 7.97 m within a 135-second outage period and a 3D Root RMSE of 5.81 m. These outcomes underscore the system's proficiency in offering accurate and dependable outdoor localisation solutions, even in the absence of GNSS signals. Moreover, Fig. 13 contrasts the ground truth flight path estimated through GNSS/INS fusion
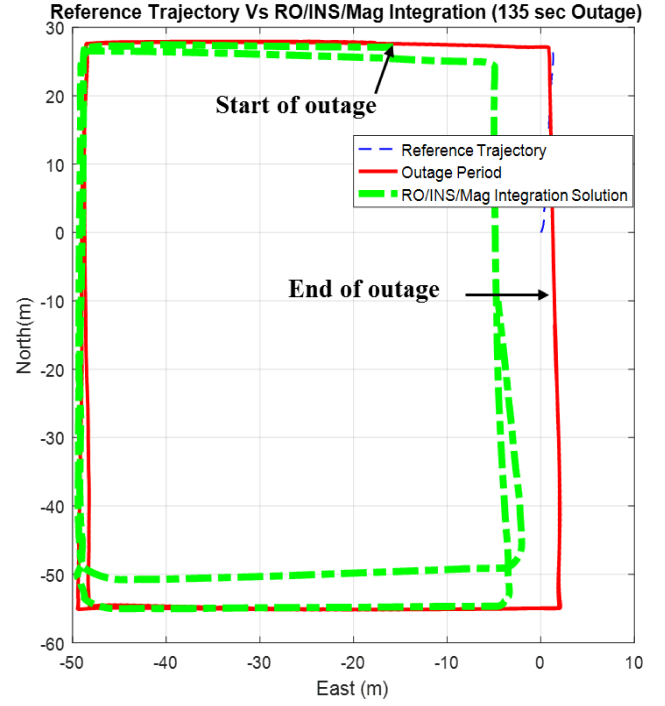
with the trajectory derived solely from INS data during a 135-second GNSS signal outage. This comparison aimed to gauge the accuracy and reliability of INS in computing flight trajectories in the absence of GNSS signals. Additionally, Fig. 14 delineates the North and East errors computed by the standalone INS over a 135-second GNSS signal outage, offering insights into the accuracy and reliability of INS in estimating the quadcopter's position during GNSS signal loss. Lastly, Fig. 15 presents a comparative analysis of the outdoor localisation system employing the RO system across various outage durations, providing a comprehensive view of its performance under different signal loss scenarios.

Table 1 presents a comparative analysis of the RMSE values obtained from the INS in the standalone mode and the RO outdoor localisation system across varying durations of GNSS signal loss. This table offers a comprehensive summary of both systems' performance in accurately estimating the quadcopter's position throughout GNSS signal loss scenarios. Furthermore, the errors in 3D positioning due to INS drift, as well as the errors in standalone mode, are notably reduced by the proposed RO-assisted outdoor localisation technique. Specifically, leveraging the EKF reduced errors to 1.19% over 45 seconds and 0.152% over 135 seconds, while employing the PF resulted in errors reduced to 1.05% over 45 seconds and 0.11% over 135 seconds. These findings indicate the effectiveness of the RO system in mitigating INS drift and minimizing outdoor localisation errors during periods of GNSS signal loss

Table 1
Comparison among the RMSE worths for the location states that are recorded from the INS and RO outdoor localisation system and the worths obtained from the ground truth.

| RMSE	Symbol		Initial Trip Outage	
			(45 sec)	(135 sec)
North direction (m)	INS Only		142.97 ± 22.7309	142.97 ± 21.0045
	Crowd-sensing System	Using EKF	1.69 ± 0.255	3.59 ± 0.524135
		Using PF	0.86 ± 0.134597	1.73 ± 0.2538
East direction (m)	INS Only		141.56 ± 22.5956	141.56 ± 20.8453
	Crowd-sensing System	Using EKF	2.17 ± 0.3167	3.90 ± 0.5753
		Using PF	1.45 ± 0.214	1.74 ± 0.2542
Height direction (m)	INS Only		221.47 ± 35.0946	221.47 ± 31.5603
	Crowd-sensing System	Using EKF	2.25 ± 0.337	2.37 ± 0.3831
		Using PF	1.21 ± 0.1894	1.67 ± 0.2453
3D Position (m)	INS Only		298.19 ± 44.8904	298.19 ± 44.2602
	Crowd-sensing System	Using EKF	3.60 ± 0.53314	5.90 ± 0.9539
		Using PF	1.89 ± 0.2939	3.87 ± 0.583679
Improvement percentages from INS (%)	Crowd-sensing System	Using EKF	98.81 ± 15.8513	99.848 ± 14.3052
		Using PF	98.95 ± 15.8032	99.89 ± 14.7816
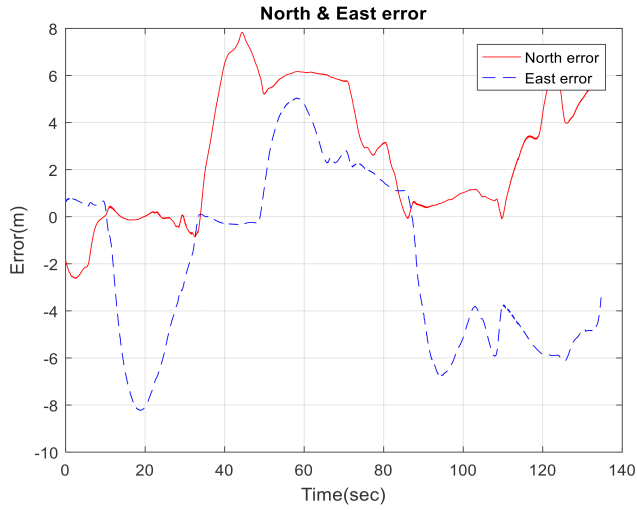
Figure 12: The North and East errors recorded by the RO-aided outdoor Localisation system during a 135-second GNSS signal loss.
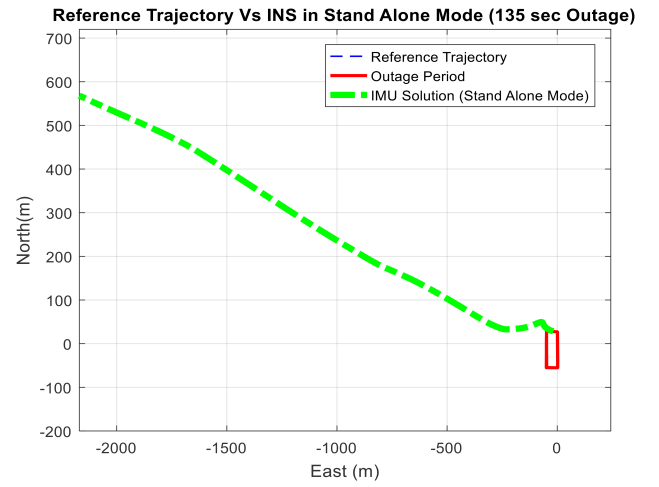

Figure 13: The differentiation between the 2D flight path loss components computed by GNSS/INS fusion versus the proposed RO integrated system in standalone mode over a 135-second duration.

4.3. The Second Experimental Trial

In the second experiment, the quadcopter traversed a diamond-shaped path encompassing thirteen waypoints over a total flight duration of 155 seconds, as depicted in Fig. 16. Fig. 17 illustrates a comparison between the reference forward velocity and the velocity computed by the RO system. The results indicated that the proposed RO outdoor localisation system effectively computed forward velocity for the quadcopter, yielding an RMSE of 2.13 m/s. Furthermore, to assess the system's resilience in mitigating GNSS signal loss effects, the performance of the RO system is evaluated in five additional outage scenarios during the second experiment. These scenarios entailed outage periods ranging from 45 seconds to 120 seconds, aimed at enhancing the robustness of the proposed outdoor localisation system against GNSS signal loss.

Fig. 18 and 19 depict the differentiation between the computed 2D flight path segments obtained from both the GNSS/INS fusion and the RO-aided outdoor localisation system during the second flight. Furthermore, Fig. 20 shows the proposed system's validation process across different GNSS signal loss periods, resulting in improved outdoor localisation solutions and a 3D RMSE of 8.14 meters within 120 seconds. Additionally, Fig. 21 presents a differentiation of the computed 2D flight path segments from the GNSS/INS fusion, while Fig. 22 illustrates the INS errors in the north and east directions. Finally, Fig. 23 highlights the variance in RMSE values for 3D positioning achieved by the RO system across various periods of GNSS signal loss.

Table 2
Differenation among the RMSE worths for the location states that are recorded from the INS and RO outdoor localisation system and the worths obtained from the ground truth.

| RMS Error (m)	Symbol		Second Trip Outage	
			(45 sec)	(120 sec)
North direction (m)	INS Only		142.97 ± 22.7281	158.98 ± 25.5574
	Crowd-sensing System	Using EKF	2.60 ± 0.3981	3.16 ± 0.4552
		Using PF	1.48 ± 0.2241	1.84 ± 0.2712
East direction (m)	INS Only		141.56 ± 22.3374	127.01 ± 18.4686
	Crowd-sensing System	Using EKF	3.30 ± 0.4858	6.79 ± 1.0008
		Using PF	1.85 ± 0.2922	3.96 ± 0.5622
Height direction (m)	INS Only		221.47 ± 32.2202	202.01 ± 28.956
	Crowd-sensing System	Using EKF	3.10 ± 0.4767	3.15 ± 0.4554
		Using PF	1.63 ± 0.2614	1.82 ± 0.282
3D Position (m)	INS Only		298.19 ± 43.423	287.01 ± 46.033
	Crowd-sensing System	Using EKF	5.20 ± 0.7434	8.13 ± 1.2115
		Using PF	2.86 ± 0.4445	5.11 ± 0.7899
Improvements percentage from INS (%)	Crowd-sensing System	Using EKF	98.18 ± 14.6156	99.67 ± 14.7921
		Using PF	98.45 ± 15.85	99.83 ± 14.5648
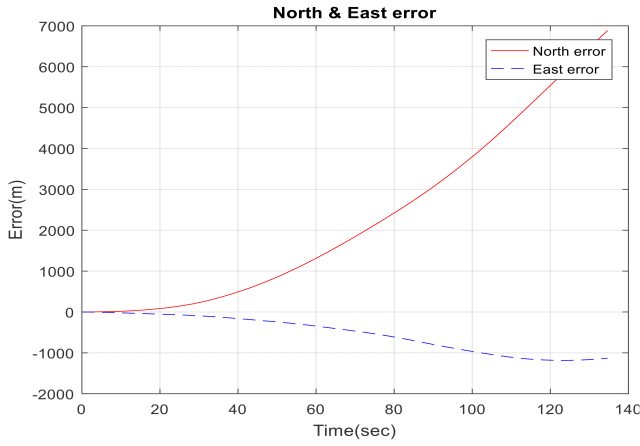
Figure 14: The North and East errors recorded by the INS in standalone mode during a 135-second interval of GNSS signal loss.
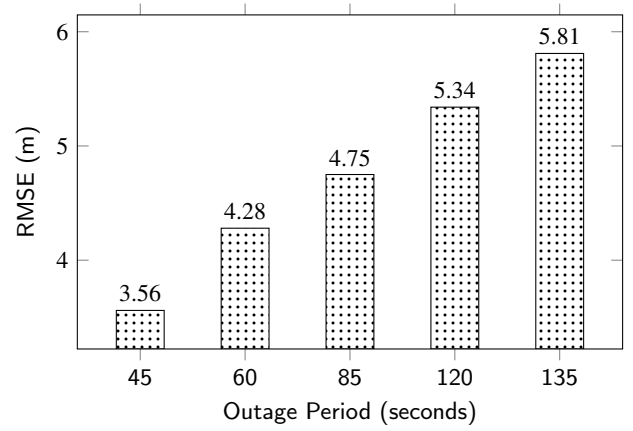

Figure 15: The RMSE of the 3D positioning measured by RO across different outage periods in an outdoor localisation system.
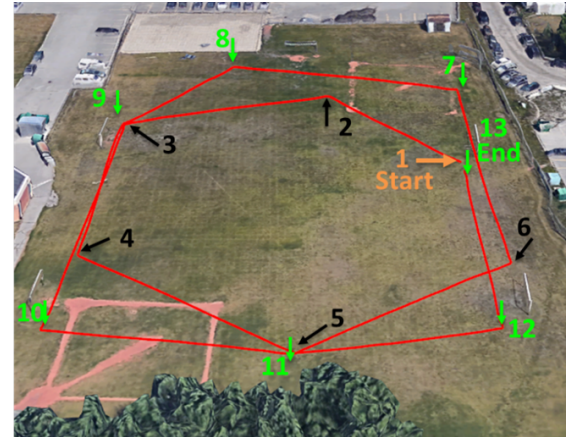
Table 2 provides a comparative analysis of the RMSE values obtained from the INS in standalone mode and the RO outdoor localisation system across various durations of GNSS signal loss. This comprehensive table offers insights into the performance of both systems concerning their capability to estimate the quadcopter's position during GNSS signal loss. Moreover, the proposed RO-assisted outdoor localisation technique significantly reduced 3D positioning errors attributed to INS drift and errors in standalone mode. Specifically, employing the EKF reduced errors to 1.82% over 45 seconds and 0.33% over 120 seconds, while utilising the PF resulted in errors reduced to 1.55% over 45 seconds and 0.17% over 120 seconds. These findings underscore the effectiveness of the RO system in mitigating INS drift and minimizing outdoor localisation errors during periods of GNSS signal loss.

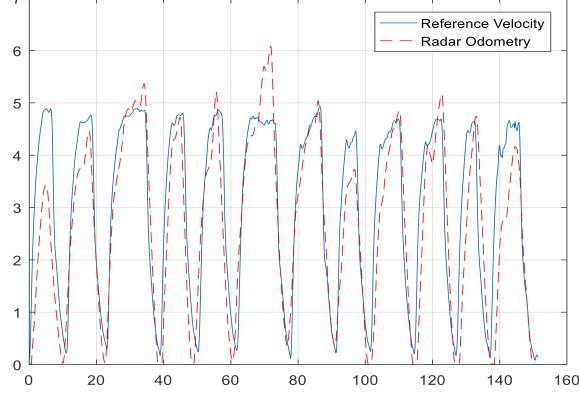

Figure 16: The waypoints of the second flight trajectory.

Figure 17: Comparison between the reference acquired velocity by the (GNSS/INS) fusion, and computed velocity by the proposed system.
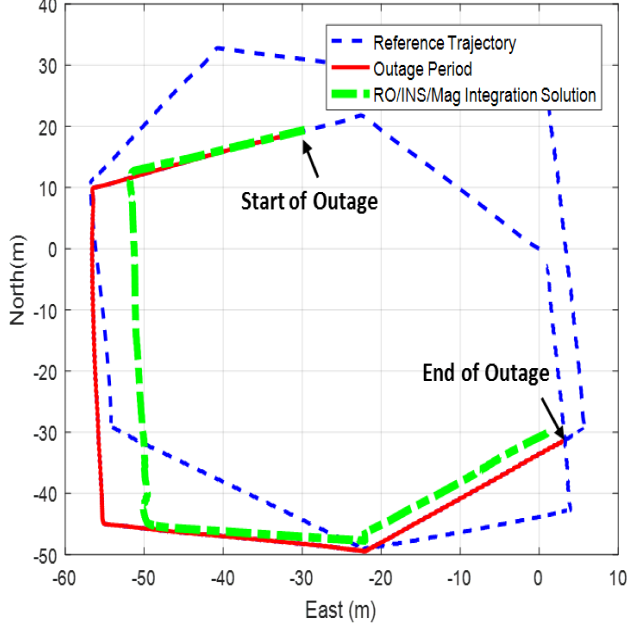
Figure 18: Differenation among the ground truth path VS the proposed RO system for 45 seconds outage.
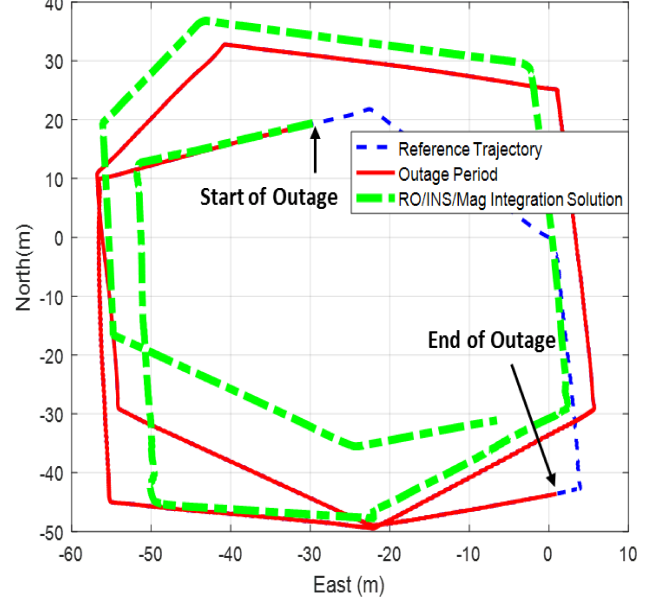

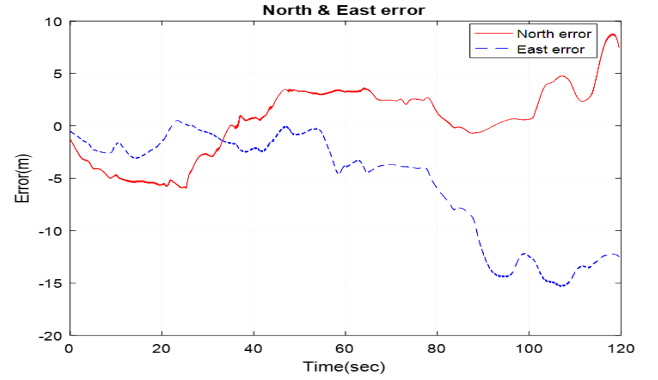**Figure 19:** Differenation among the ground truth path VS the proposed RO system for 120 seconds outage.

Figure 20: The North and East errors recorded by the RO-assisted outdoor localisation system during a 120-second GNSS outage period.

5. Conclusions

This paper introduces a pioneering strategy leveraging RO to significantly enhance the precision and reliability of outdoor localisation systems for UAVs during GNSS outages. The proposed system integrates an FMCW radar, crucial for capturing ground object range-Doppler maps to derive scatterers' radial velocities, forming the backbone of data capture, target identification, and velocity extraction processes. Employing linked component methods and adaptive thresholding, the target detection technique enhances accuracy and dependability during GNSS signal failures.

Integration of forward velocity from fused crowd-sensing measurements with INS data using nonlinear estimators like EKF and PF further boosts localisation precision and reliability during GNSS signal losses. Notably, this approach operates in real-time, without relying on artificial reflectors, utilising natural scatterers. It accounts for object reflectance variations, considers sensor-vehicle frame disparities, and addresses IMU measurement uncertainties. Evaluation through flights featuring various manoeuvres, including deliberate GNSS outages, demonstrates significant INS precision improvements, averaging 99.89% in 3D positioning for the initial trip and 99.83% for the second trip when using PF. These outcomes underscore the effectiveness of the RO-assisted method in enhancing UAV
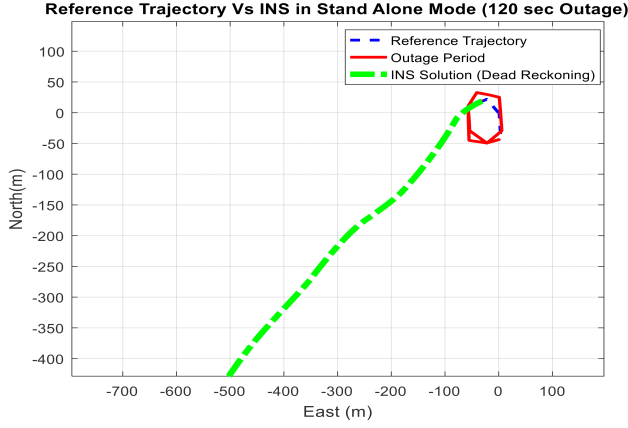
Figure 21: The differentiation between the 2D flight path loss components computed by GNSS/INS fusion versus the proposed RO integrated system in standalone mode over a 120-second duration.
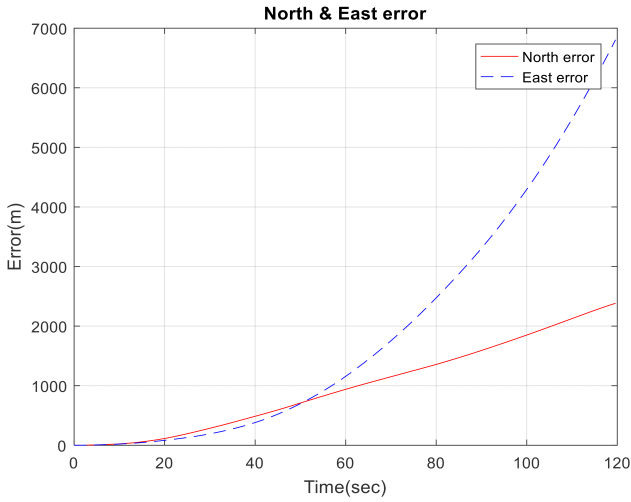

Figure 22: The North and East errors recorded by the INS in standalone mode during a 135-second interval of GNSS signal loss.

outdoor localisation reliability and accuracy, particularly under challenging GNSS signal loss scenarios facilitated by the application of nonlinear estimators like EKF and PF. This method showcases promise for real-world application in UAV localisation, showcasing considerable improvements in precision and reliability, which is pivotal for navigating GNSS-challenged environments.
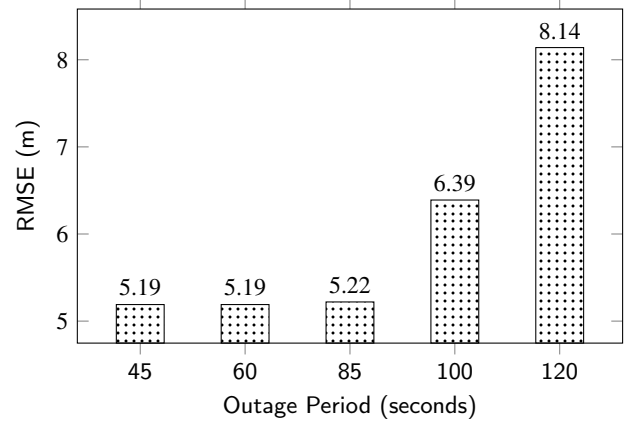

Figure 23: The RMSE of the 3D positioning measured by RO across different outage periods in an outdoor localisation system.

References

[1] E. B. Quist and R. W. Beard, Radar odometry on fixed-wing small unmanned aircraft, *IEEE Transactions on Aerospace and Electronic Systems*, 52(1), 396–410, (2016, February).

[2] E. B. Quist, P. C. Niedfeldt, and R. W. Beard, Radar odometry with recursive-RANSAC, *IEEE Transactions on Aerospace and Electronic Systems*, 52(4), 1618–1630, (2016, August).

[3] W. Sun, G. C. Zhang, X. R. Zhang, and X. Zhang, Fine-grained vehicle type classification using lightweight convolutional neural network with feature optimization and joint learning strategy, *Multimedia Tools and Applications*, 80(4), 30803–30816, (2021, July).

[4] C. Forster, M. Pizzoli, and D. Scaramuzza, SVO: Fast semi-direct monocular visual odometry, IEEE International Conference on Robotics and Automation, USA, 15-22, (2014).

[5] H. Masood, A. Zafar, M. U. Ali, M. A. Khan, S. Ahmed, et al., Recognition and tracking of objects in a clustered remote scene environment, *Computers, Materials & Continua*, 70(1), 1699–1719, (2021, September).

[6] M. Blösch, S. Weiss, D. Scaramuzza, and R. Siegwart, Vision-based MAV navigation in unknown and unstructured environments, IEEE International Conference on Robotics and Automation, Anchorage, AK, USA, 21–28, (2010).

[7] M. Bryson, M. Johnson-Roberson, and S. Sukkarieh, Airborne smoothing and mapping using vision and inertial sensors, IEEE International Conference on Robotics and Automation, Kobe, Japan, 2037-2042, (2009).

[8] A. Gamal, M. Mostafa, A. Masiero, A. Zaghloul, M. Naser, et al., Indoor positioning system based on magnetic fingerprinting image, *Bulletin of Electrical Engineering and Informatics*, 10(3), 1325–1336, (2021).

[9] W. Sun, X. Zhang, and X. He, Lightweight image classifier using dilated and depthwise separable convolutions, *Journal of Cloud Computing: Advances, Systems, and Applications*, 9(1), 1–12, (2020).

[10] K. C. Huang, S. H. Tseng, W. H. Mou, and L. C. Fu, Simultaneous localization and scene reconstruction with monocular camera, in IEEE International Conference on Robotics and Automation, USA, 2–7, (2012).

[11] G. Klein, and D. Murray, Parallel Tracking and Mapping for Small AR Workspaces, $6^t h$ IEEE and ACM International Symposium on Mixed and Augmented Reality, 225–234, (2007).

[12] W. Sun, Y. T. Du, X. Zhang, and G. C. Zhang, Detection and recognition of text traffic signs above the road, *International Journal of Sensor Networks*, 35(2), 69-77, (2021, March).

[13] H. Strasdat, J. M. M. Montiel, and A. J. Davison, Real-time monocular SLAM: Why filter? in IEEE International Conference on Robotics

and Automation, Anchorage Convention District, Anchorage, Alaska, USA, 2657–2664, (2010).

[14] W. Sun, M. Sun, X. Zhang, and M. Li, Moving vehicle detection and tracking based on optical flow method and immune particle filter under complex transportation environments, *Complexity*, 2020(16), 1–15, (2020, April).

[15] Z. A. Ali, H. Zhangang, and W. B. Hang, Cooperative path planning of multiple UAVs by using max–min ant colony optimization along with Cauchy mutant operator, *Fluctuation and Noise Letter*, 20(1), (2021).

[16] D. Eynard, P. Vasseur, C. Demonceaux, and V. Frémont, UAV altitude estimation by mixed stereoscopic vision, *IEEE/RSJ International Conference on Intelligent Robots and Systems*, Taiwan, 646–651, (2010).

[17] T. B. Karamat, R. G. Lins, S. N. Givigi, and A. Noureldin, Novel EKF-Based Vision/Inertial System Integration for Improved Navigation, *IEEE Transactions on Instrumentation and Measurement*, 67(1), 116-125, (2018, January).

[18] P. Raja and S. Pugazhenthi, Optimal path planning of mobile robots: A review, *International Journal of Physical Sciences*, 7(9), 1314–1320, (2012, February).

[19] H. Fiyad, A. Gamal, M. Mostafa, A. Zaghloul, M. Naser, et al., An improved real visual tracking system using particle filter, *Przeglad Electrotechniczny*, 11(1), 164–169, (2021).

[20] D. I. Vilaseca, and J. I. Giribet, Indoor navigation using WiFi signals, in *4th Argentine Symposium and Conference on Embedded Systems (SASE/CASE)*, Argentina, 1–6, (2013).

[21] K. Ali, A. N. Quershi, A. Alauddin, M. S. Bhatti, A. Sohail, et al., Deep image restoration model: A defense method against adversarial attacks, *Computers, Materials & Continua*, 71(2), 2209–2224, (2022).

[22] A. Gamal, M. Saleh, and A. Elmahallawy, De-noising of Secured Stego-Images using AES for Various Noise Types, *Przeglad Electrotechniczny*, 2(2), 21–26, (2023).

[23] A. Gasparetto, P. Boscariol, A. Lanzutti, and R. Vidoni, Path planning and trajectory planning algorithms: A general overview, *Motion and Operation Planning of Robotic Systems*, 29(2015), 3–27, (2015).

[24] R. Raquet, F. John, M. Miller, M. Mikel, and T. Q. Nguyen, Issues and Approaches for Navigation Using Signals of Opportunity, Proceedings of the National Technical Meeting of The Institute of Navigation, San Diego, Canda, 1073-1080, (2007).

[25] M. Achtelik, S. Weiss, and R. Siegwart, Onboard IMU and monocular vision based control for MAVs in unknown in- and outdoor environments, IEEE International Conference on Robotics and Automation, Shanghai, China, 3056–3063, (2011).

[26] E. Zaugg, D. Hudson, and D. Long, The BYU SAR: A Small, Student-Built SAR for UAV Operation, in IEEE International Symposium on Geoscience and Remote Sensing, pp. 411–414, (2006).

[27] K. Kauffman, J. Raquet, Y. Morton, and D. Garmatyuk, Real-Time UWB-OFDM Radar-Based Navigation in Unknown Terrain, *IEEE Transactions on Aerospace*, 49(3), 1453–1466, (2013, July).

[28] E. B. Quist and R. Beard, Radar Odometry on Small Unmanned Aircraft, in *Guidance, Navigation, and Control (GNC) Conference*, USA, 4698-4716, (2013, August).

[29] J. Rehder, K. Gupta, S. Nuske, and S. Singh, Global pose estimation with limited GPS and long-range visual odometry, IEEE International Conference on Robotics and Automation, USA, 627–633, (2012).

[30] A. Gamal, A. Salama, H. Zied, A. Elmahallawy, and M. A. Shawky, An improved indoor positioning based on crowd-sensing data fusion and particle filter, *Physical Communication*, 61, (2023, November).

[31] J. Kaur, M. Shawky, M. S. Mollel, O. R. Popoola, M. A. Imran, Q. H. Abbasi, and H. T. Abbas, AI-enabled CSI fingerprinting for indoor localisation towards context-aware networking in 6G, IEEE Wireless Communications and Networking Conference (WCNC), Glasgow, United Kingdom, 1-5, (2023).

[32] S. T. Shah, M. A. Shawky, J. U. Kazim, A. Taha, S. Ansari, S. F. Hasan, M. A. Imran, and Q. H. Abbasi, Coded environments: data-driven indoor localisation with reconfigurable intelligent surfaces,

Communications Engineering, 3(66), (2024, May).

[33] K. Karunanithy, and B. Velusamy, Directional antenna based node localization and reliable data collection mechanism using local sink for wireless sensor networks, *Journal of Industrial Information Integration*, 24(1), (2021).

[34] X. Kong, C. Wu, Y. You, and Y. Yuan, Hybrid indoor positioning method of BLE and PDR based on adaptive feedback EKF with low BLE deployment density, *IEEE Transactions on Instrumentation and Measurement*, 72, 1-12, (2022, December).

[35] A. F. Scannapieco, A. Renga, G. Fasano, and A. Moccia, Ultralight radar sensor for autonomous operations by micro-UAS, International Conference on Unmanned Aircraft Systems (ICUAS), USA, 727–735, (2016).

[36] H. Zied, A. Gamal, and A. Salem, S-Box Modification for the Block Cipher Algorithms, *Przeglad Electrotechniczny*, 4(4), 278–281, (2023).

[37] S. Said, S. Kork, T. Beyrouthy, M. Hassan, O. Abdellatif, et al., Real-time eye tracking and detection—A driving assistance system, *Advances in Science, Technology and Engineering Systems Journal*, 3(6), 446–454, (2018).

[38] R. Miller, Fundamentals of Radar Signal Processing, *IEEE Signal Processing Magazine*, 26(3), 100-101, (2009, May).

[39] L. Wang, M. J. Er, and S. Zhang, A kernel extreme learning machines algorithm for node localization in wireless sensor networks, *IEEE Communications Letters*, 24(7), 1433–1436, (2020, July).

[40] M. Mostafa, S. Zahran, A. Moussa, N. El-Sheimy, and A. Sesay, Radar and visual odometry integrated system aided navigation for UAVs in GNSS denied environment, *Sensors*, 18(9), (2018).

[41] S. Zahran, M. Mostafa, A. Moussa, and N. El-Sheimy, Augmented Radar Odometry by Nested Optimal Filter Aided Navigation for UAVs in GNSS Denied Environment, *International Telecommunications Conference, ITC-Egypt*, 1-5, (2021).

Mostafa Mohamed Ahmed received his B.Sc. degree (with honours) in Communication and Electrical engineering and the M.Sc. degree in Electrical engineering from Alexandria University, Alexandria, Egypt, in 2005 and 2013, respectively, and the Ph.D. degree in electrical, computer, and geomatics engineering from the University of Calgary, Calgary, AB, Canada, in 2017. He is currently a doctor at the Air Defense College, Alexandria, Egypt and a research assistant in the Mobile Multi-Sensor Systems (MMSS) Research Group, Department of Geomatics, University of Calgary. He has experience in Unmanned Aerial Vehicles (UAVs) navigation systems, His research interests include Global Navigation Satellite System (GNSS) denied environment navigation systems for UAVs, low-cost multi-sensors fusion, machine learning, adaptive digital signal processing, radar signal processing, advanced estimation techniques, computer vision, and image processing.

Mahmoud A. Shawky was born in 1990 in Saudi Arabia. He received his B.Sc. degree in Electronics and Electrical Engineering in 2012 from Air Defence College, Alexandria University, M.Sc. (Eng.) degree in Authentication Mechanisms in Computer Network Protocols from Alexandria University, Alexandria, Egypt. He received his PhD degree from the James Watt School of Engineering, University of Glasgow, UK. His research interests are in the areas of cryptography and number theory, digital signatures, authentication in wireless communications and cyber security.

Shady Zahran has a PhD degree in electrical, computer, and geomatics engineering from the University of Calgary, Calgary, AB, Canada. He received his M.Sc. in Communication and Electrical Engineering at Ain Shams University, Cairo, Egypt, in 2016. He is a research assistant in the Mobile Multi-Sensor Systems (MMSS) Research Group, Department of Geomatics, University of Calgary. He has experience in UAVs, UGVs, and UAS. His research interests include indoor and outdoor navigation in harsh environments, low-cost multi-sensor integration, and embedded systems.

Adel Mohamed Moussa received his PhD degree in electrical, computer, and geomatics engineering from the University of Calgary, Calgary, AB, Canada, in 2013. He received his M.Sc. and B.Sc. in Computer Engineering from Port-Said University, Egypt, in 2013. He is currently a post-doctor scholar in the Mobile Multi-Sensor Systems (MMSS) Research Group, Department of Geomatics, University of Calgary. His research interests include image processing, artificial intelligence, remote sensing, photogrammetry, indoor and outdoor navigation, mapping, low-cost multi-sensors integration.

Naser El-Sheimy received his B.Sc. degree (with honours) in civil engineering and the M.Sc. degree in surveying engineering from Ain Shams University, Cairo, Egypt, in 1984 and 1990, respectively, and the PhD degree in geomatics Conf. Scientific papers. His current research interests include; Speech and Audio Coding, Packet voice transmission over data networks, wireless communication systems and networking security. He was the Vice Chairman of the Twenty-Fifth National Radio Science Conference (NRSC,2008), Tanta, Egypt. During the period from 2006 to 2009, he was the President of the Administration Board for the Information and Communication Technology Project (ICTP) at Tanta University and led the technical team to manage and modify the Tanta University network. From Sept. 2009 chief Information officer (CIO) and coordinator at Tanta University until Jan 2010. From Feb. 2010 tell Aug. 2014. He was the Dean of Ras EL-Bar Higher Institute for Computers, Damietta and. from Sep. 2014 tell Aug. 2016, Dean of Alex. Higher Institute of Eng, & Technology, Alex., Egypt.

Dr. Adham Ahmed Elmahallawy is a highly qualified lecturer with a strong background in Communications, Electronics, and Electro Physics Engineering. He earned his Bachelor's degree with distinction and honors from Alexandria University in 1994. He has also completed several technical courses in electronic and communications engineering design and implementation. In 2001, Dr. Elmahallawy obtained his Master's degree in Electrical Engineering from Alexandria University. He went on to pursue his Doctor of Philosophy degree in electrical engineering, which he earned from the Department of Electronics and Communications Engineering at the University of Alexandria in 2010. Also, he has published different research papers in highly-rated journals. He currently serves as a lecturer at the Higher Institute of Engineering and Technology, King Mariout, Alexandria, Egypt.

Shuja Ansari is a Lecturer in the Glasgow College UESTC at the University of Glasgow, UK. He received the M.Sc. degree (distinction) in Telecommunications Engineering in 2015, and the Ph.D. degree in Engineering in 2019 from Glasgow Caledonian University (GCU), UK. He joined the Communications, Sensing and Imaging research group at the University of Glasgow as a Research Associate in 2019 working on energy-efficient 5G mobile networks. He is currently the Wave-1 Urban 5G use case implementation lead at Glasgow 5G Testbed funded by the Scotland 5G Centre of the Scottish Government working on a variety of 5G applications in partnership with several industrial and academic partners. His research interests include Wireless Communications, Internet of Things, Cooperative Intelligent Transport Systems, Autonomous Systems, Terrestrial/Airborne Mobile Networks, and Healthcare technologies.

Syed Tariq Shah is a highly accomplished academic and research professional with a background in Electrical and Electronic Engineering. He received his Master's and Ph.D. degrees from the Department of Electrical and Electronic Engineering at Sungkyunkwan University in Suwon, South Korea, in 2015 and 2018, respectively. Currently, he is working as a Postdoctoral Fellow at the University of Glasgow in the UK and also serving as an Associate Professor with the Department of Electrical Engineering, BUITEMS, Pakistan. His research interests include 5G and beyond networks, Open RAN, AI-enabled wireless networks, RF energy harvesting, and Intelligent reflecting surfaces. Dr Shah is also an Editor of the Electronics Journal and a reviewer of several IEEE Transactions, Letters, and Magazines.

Ahmed Gamal Abdellatif Ibrahim is a dedicated lecturer in the Department of Communications and Electronics Engineering at the Air Defense College in Alexandria, Egypt. He was born in 1985 in Sharkia Governorate, Egypt. In 2007, Dr Gamal graduated with a B.Sc. degree with honours in Electronics and Electrical Engineering from the Air Defense College at Alexandria University. He continued his academic journey and obtained a master's degree in Electronics and Electrical Engineering from Alexandria University in 2017. Dr. Gamal has also demonstrated his commitment to expanding his knowledge and gaining international experience. In 2019, he became a PhD student visitor at the prestigious Research Center of Geomatics (CIRGEO) at the University of Padua in Italy. This valuable experience allowed him to broaden his horizons and enrich his research pursuits. Dr. Gamal successfully completed his PhD degree in Electronics and Communications Engineering in 2022. His research interests reflect his diverse background and multidisciplinary approach, including navigation, indoor positioning, tracking, filtering, information security, and image processing. Finally, He is a reviewer for several journals and flagship conferences.